Optimization and Active Stabilization of a Far-Infrared Laser for NSTX-U High Poloidal Wavenumber Scattering Diagnostics

Xinhang Xu[1], Jon Dannenberg[1], Calvin Domier[1], Yilun Zhu[1], Xiaoliang Li[1,a)], Neville Luhmann, Jr. [1] and Yang Ren[2]

[1]*University of California, Davis, Davis, California, 95616*

[2]*Princeton Plasma Physics Laboratory, Princeton, New Jersey, 08540*

a) Authors to whom correspondence should be addressed: bxlli@ucdavis.edu

ABSTRACT

The far-infrared (FIR) laser output beam power and profile are important parameters in the laser-aided diagnostics, directly influencing the spatial resolution and signal-to-noise ratio of measurements. This work focuses on developing a systematic control method to enhance FIR laser beam quality through optimized mirror alignment and real-time feedback-based precision cavity length tuning. A 150 W CO_2 laser, aligned with the waveguide axis using a HeNe reference laser, serves as the pump source. The sensitivity of FIR beam intensity to pump gas pressure and thermal expansion is investigated, revealing that even a 1 µm cavity expansion can significantly degrade output power stability to about two-thirds of its original value. To address this, a feedback control module has been designed and implemented for active cavity length adjustment, stabilizing the output power at approximately 30 mW. Additionally, maintaining a high formic acid gas pressure (> 190 mTorr) within the cavity ensures reliable operation. The optimized FIR laser will be deployed on the NSTX-U high poloidal wavenumber scattering system for studying electron-scale turbulence in tokamak plasmas.

I. INTRODUCTION

Transport is one of the top-level research topics in fusion plasma physics[1, 2]. In H-mode plasmas in the National Spherical Torus eXperiment (NSTX) device[3], electron thermal transport has been observed to exceed the corresponding neoclassical transport prediction by a significant margin[4, 5], while ion thermal transport is at the neoclassical level. This elevated electron thermal transport can lead to a substantial thermal loss and degraded energy confinement[6, 7]. Consequently, understanding and controlling electron thermal transport is critical for predicting and optimizing confinement of future magnetic confinement devices with dominant electron heating. Electrons-scale turbulence has been considered as a major candidate in driving electron thermal transport[5, 8, 9]. The NSTX-U device[10], with its distinctive high-beta and low-collisionality condition, provides an ideal platform for investigating electron-scale turbulence, where turbulence characteristics vary with essential parameters such as collisionality, the q-profile, and E × B shear, aiming to identify the mechanisms that govern the Spherical Tokamak (ST) energy confinement scaling[4, 11].

An essential diagnostics system in this investigation is the 693 GHz, 8-channel millimeter-wave poloidal scattering system[12-14] , which will measure electron-scale turbulence across the plasma core to edge (normalized radius ρ from 0.2 to 1) with a poloidal wavenumber range of 7 to ~40 cm^{-1}. This capability enables comprehensive coverage of the predicted electron temperature gradient (ETG)[15] and other electron-scale turbulence spectra. Compared to millimeter-wave diagnostics[16-23], laser-aided diagnostics provide enhanced spatial resolution and wider wavenumber range. The system utilizes an

optically pumped far-infrared (FIR) laser with formic acid (HCOOH) vapor serving as the gain medium. It is pumped by a 150 W CO_2 laser operating on the 9R20 line (wavelength = 9.27 μm), which drives rotational transitions to generate the 693 GHz FIR signal[24]. The output beam is coupled into a waveguide and directed to the launch optics, where adjustable mirrors allow precise beam steering for various measurement configurations. Compared to millimeter-wave diagnostics[25-28], laser-aided diagnostics involve more complex optical systems, necessitating finer adjustments and stricter maintenance requirements[29]. Maintaining a high-quality Gaussian beam profile is essentially required for efficient waveguide coupling[30]. This depends sensitively on the precise alignment of FIR cavity components, including perforated copper mirrors, mesh grids, and dielectric wafers. Even minor misalignments (as small as 0.1°) can significantly degrade the output beam quality. Additionally, heat from the CO_2 laser can alter the length of the FIR laser cavity, resulting in a drop in output power. This work addresses these challenges by developing a repeatable alignment methodology and identifying the key factors that govern beam patterns and power optimization in FIR systems.

This paper focuses on optimizing the performance of a 693 GHz far-infrared (FIR) laser through precision optics alignment and cavity length feedback control. The beam quality of the FIR laser system, which is driven by a CO_2 pump laser, is important for high poloidal wavenumber scattering diagnostics. Section 2 reviews the FIR laser setup, while Sec. 3 presents beam profile optimization by optics alignment. Section 4 details power stabilization through real-time cavity length feedback control and gas pressure tuning. Finally, Sec. 5 summarizes the implications for improving FIR laser stability and output efficiency.

II. FIR LASER SETUP AND BEAM QUALITY IMPORTANCE

The 693 GHz far-infrared laser serves as the launch beam source for the NSTX-U high-k scattering diagnostics. This laser is optically pumped by a 150 W CO_2 laser with a linearly polarized beam. The CO_2 laser beam is injected into the FIR laser cavity, which is filled with formic acid gas as the gain medium, as shown in Fig. 1.
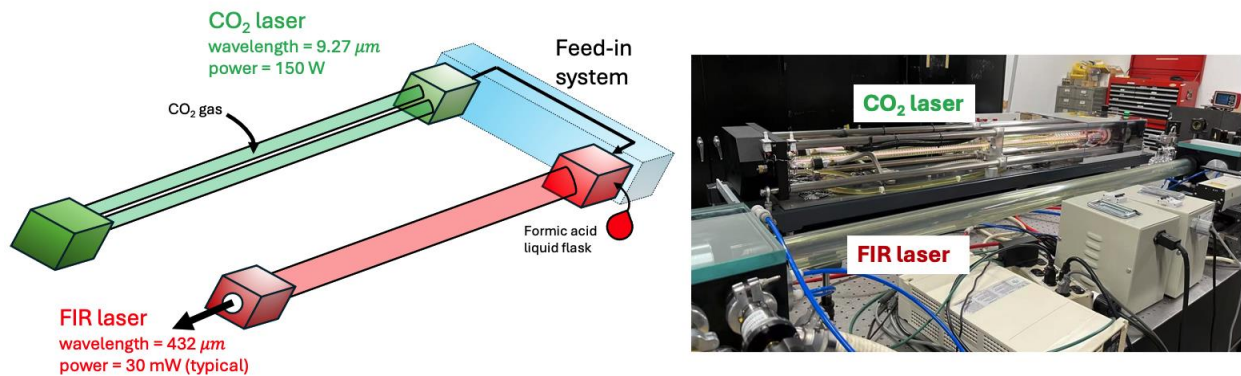

Figure 1. (left) The formic acid FIR laser is driven by a 150 W CO_2 laser through feed-in system pumping. (right) The laser system setup in the laboratory.

The CO_2 laser, as shown in Fig. 2, features two independent waveguide cavities, each powered by a dedicated high-voltage supply (-15 kV cathode, 0 V anode) that initiates gas breakdown in the CO_2-N_2-He mixture (6:18:76 ratio). This discharge sustains a 40 mA plasma current that excites CO_2 molecules,

producing infrared radiation through quantum cascade transitions[31]. The system employs Brewster windows to enforce P-polarization (100% transmission) while suppressing S-polarization through reflection and absorption. Wavelength selection is achieved via a tunable diffraction grating, which together with the output coupler's ZnSe mirror (60% reflectivity at 10 μm) forms the complete laser cavity. Resonant feedback between these components stimulates continuous laser action, with maximum output occurring when the cavity length satisfies the standing wave condition.
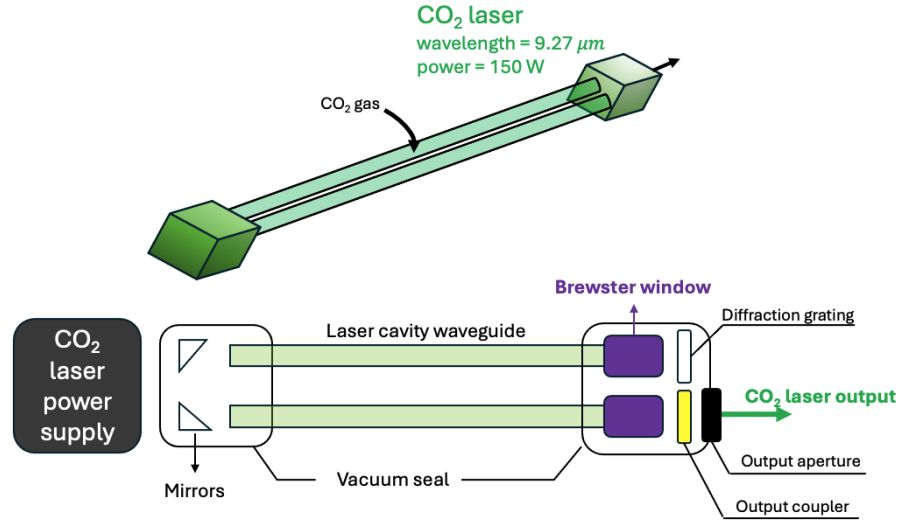

Figure 2. Schematic of the CO₂ laser. The main components include the output coupler, Brewster windows, diffraction grating, and laser cavity waveguide.

The schematic of the FIR system is presented in Fig. 3. It comprises four key components: a rear mirror, a laser cavity waveguide, a front mirror, and a metallic mesh. The rear mirror consists of a gold-coated copper substrate with a central aperture for CO_2 laser beam injection. Opposite this, the front mirror employs a dielectric-coated silicon wafer optimized for dual functionality, while achieving 98% transmission in the FIR range and reflecting 99% of the incident CO_2 laser radiation. The system incorporates a 300 lpi (line per inch) metallic mesh that exhibits wavelength-selective behavior, transmitting 20% and reflecting 80% of the 432 μm FIR radiation. These optical elements are contained within the FIR laser system, forming the complete resonant cavity structure.
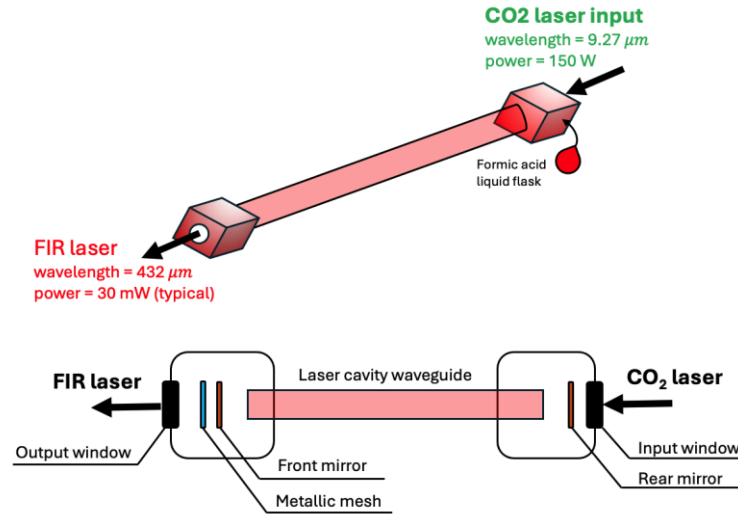
Figure 3. Schematic of the FIR laser. The main components include the front/rear mirror, metallic mesh, and laser cavity waveguide.

Figure 4 presents a schematic of the feed-in system, detailing the optical path and key components including steering mirrors, focusing lens, beam splitter, and power monitor. The CO_2 laser beam is directed into the FIR laser cavity via two adjustable mirrors that precisely align its propagation axis. A 1 m focal length focusing lens collimates the beam before it enters through the input coupler window. Inside the cavity, a copper mirror with a 4 mm radius central aperture is positioned such that the CO_2 laser beam waist coincides with the aperture location. This strategic placement allows for controlled beam expansion within the FIR cavity while minimizing back-reflected power that could interfere with CO_2 laser stability. For real-time power monitoring, a beam splitter samples 5% of the incident CO_2 laser radiation, diverting it to a calibrated detector while maintaining the primary beam path integrity.

Operating on molecular rotational transitions, the FIR laser emits submillimeter-wave radiation at approximately 693 GHz with ~ 30 mW output power. This frequency is carefully chosen to ensure that the laser beam can propagate through the plasma without significant refraction or absorption, even in high-density scenarios (0.5×10^{20} $/m^3$). The FIR laser output beam will be coupled with the transmission line through coupling optics lenses.
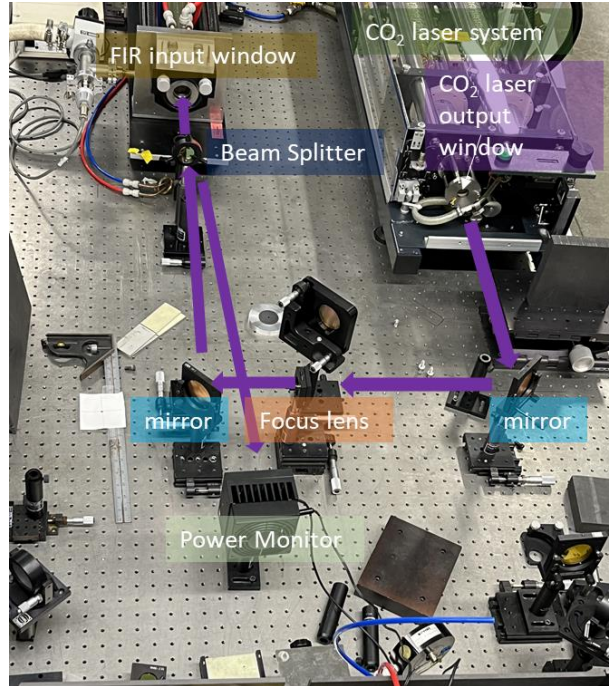
waveguide.

Figure 4. Feed-in system between CO_2 laser and FIR laser.

The NSTX-U high-k scattering diagnostics require a 693 GHz beam with at least 10 mW power at the transmission line's end (near the NSTX-U window) to achieve a signal-to-noise ratio greater than 10. The high-k scattering system launch beam laser stands in the laser cage area, as shown in Fig. 5, which is far away from the NSTX-U vessel. The long-distance (20 m) waveguide is used as the transmission line for launch beam delivery, which requires a high-quality coupling beam profile for insertion loss minimization. Ensuring a high-quality FIR laser output beam profile is essential for maximizing coupling efficiency across the transmission line, which includes the coupling optics and long-distance beam propagation. As demonstrated in Perkins[30], the highest coupling efficiency between the FIR output and the transmission line waveguide is achieved when the beam profile approximates a Gaussian fundamental mode aligned with the EH_{11} waveguide mode. The FIR output beam profile is primarily determined by FIR laser internal mirror alignment and the laser output window condition. Using a Gaussian beam input for the transmission line waveguide preserves the Gaussian profile at the output, thereby improving the spatial resolution of high-k scattering measurements. This approach streamlines the launch optics design near the NSTX-U window and provides closer agreement with synthetic diagnostics simulations[14].
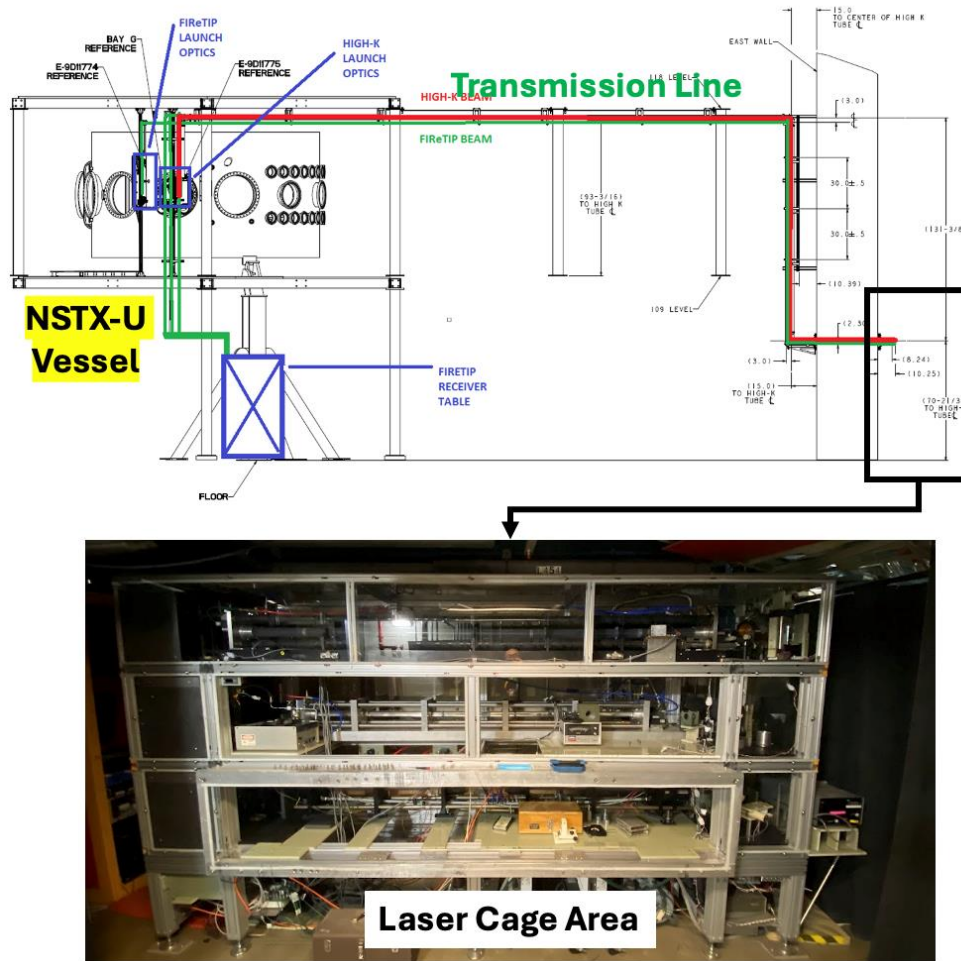
Figure 5. The FIR laser is generated at the laser cage area, then transmits to the NSTX-U vessel through transmission line waveguides. The red line stands for the high-k scattering beam transmission line.

On the other hand, the stability of the FIR laser output power is critical for ensuring reliable, high-k scattering diagnostics performance. The FIR laser typically delivers ~ 30 mW of output power, which depends on several factors: the CO_2 laser input power, FIR cavity length, gas pressure, and internal mirror alignment (CO_2 laser and FIR laser). Laboratory characterization shows that the CO_2 laser input power stabilizes after a 1-hour warm-up period, making it a reliable driver for the FIR laser. The FIR cavity length (the most sensitive parameter) is susceptible to thermal expansion effects, leading to output power fluctuations during extended operation. While gas pressure and mirror alignment remain stable after initial setup, real-time monitoring and feedback control of the FIR output power are essential to maintain stability over standard 8-hour operational periods.

III. FIR LASER OUTPUT BEAM PROFILE OPTIMIZATION

The FIR laser output beam profile and power are determined by the alignment of the metallic mesh, front mirror, and rear mirror. Proper alignment requires that the normal vectors of these components be precisely oriented along the optical axis of the laser cavity. When this condition is met, the output beam adopts the HE_{11} mode profile. Furthermore, maximum output power is achieved when the cavity length

satisfies the resonance condition for optimal lasing efficiency. Given the planar geometry of all three optical elements, the dominant installation errors are tilt angle misalignments. These tilt errors induce higher-order modes, causing the beam profile to deviate from the ideal Gaussian distribution and significantly reducing the FIR beam's coupling efficiency into the transmission line.

During initial alignment, non-ideal beam profiles (e.g., the donut-shaped mode in Fig. 6 with a central power null) frequently appear, indicating higher-order mode excitation instead of the target Gaussian mode. This mismatch reduces waveguide coupling efficiency by > 20 %, underscoring the need for precise alignment to suppress higher-order modes.
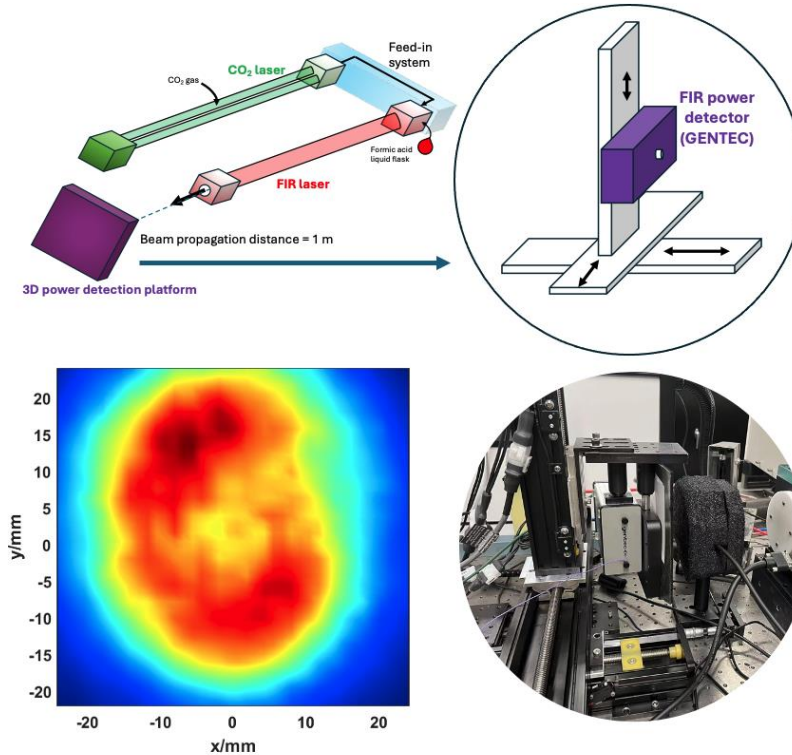

Figure 6. Donut-shaped beam profile of the FIR laser measured 1 meter from the output window.

The alignment process begins by establishing the optical axis using a visible HeNe laser. First, all internal components (mirrors, mesh, and input/output windows) are removed, leaving only the bare laser waveguide. Two precisely machined black Delrin guides with centered pinholes are then installed at each waveguide end to provide alignment references. The HeNe laser is carefully adjusted until its beam passes concentrically through both guide pinholes and the aim center of the image plane, thereby defining the system's optical axis. The distance between the imaging plane and the output window is approximately 3.5 m, ensuring high-precision tilt angle alignment in 0.1 degree. Following this, the guides are removed and the rear mirror (a gold-coated copper substrate with a central CO_2 laser injection aperture, marked as # 1) is installed. The reflected HeNe beam produces Fraunhofer diffraction rings on the image plane, where the ring center indicates the mirror's tilt angle alignment. Final adjustment is achieved when the diffraction pattern center coincides with the original HeNe reference beam location, ensuring proper mirror alignment with the established optical axis.

The front mirror (designated as # 2 in Fig. 7) utilizes a dielectric-coated silicon wafer engineered for dual-band performance: 98% transmission at FIR wavelengths and 99% reflectivity for CO_2 laser radiation. Alignment verification is performed using the HeNe laser, where proper orientation is achieved when the reflected spot coincides precisely with the reference aim center on the image plane. The metallic mesh (labeled # 3 in Fig. 7), incorporating a 300 lines-per-inch (lpi) grid, forms the FIR laser cavity together with the rear mirror. This wavelength-selective component reflects 80% and transmits 20% of the 432 μm FIR radiation. Following the front mirror installation, the mesh is aligned using the HeNe laser beam, which produces a grating diffraction pattern upon reflection. Precise tilt angle adjustment of the mesh allows controlled positioning of the zeroth-order diffraction spot on the image plane. Final alignment is achieved when this central diffraction spot coincides exactly with the reference aim center, ensuring optimal cavity performance.
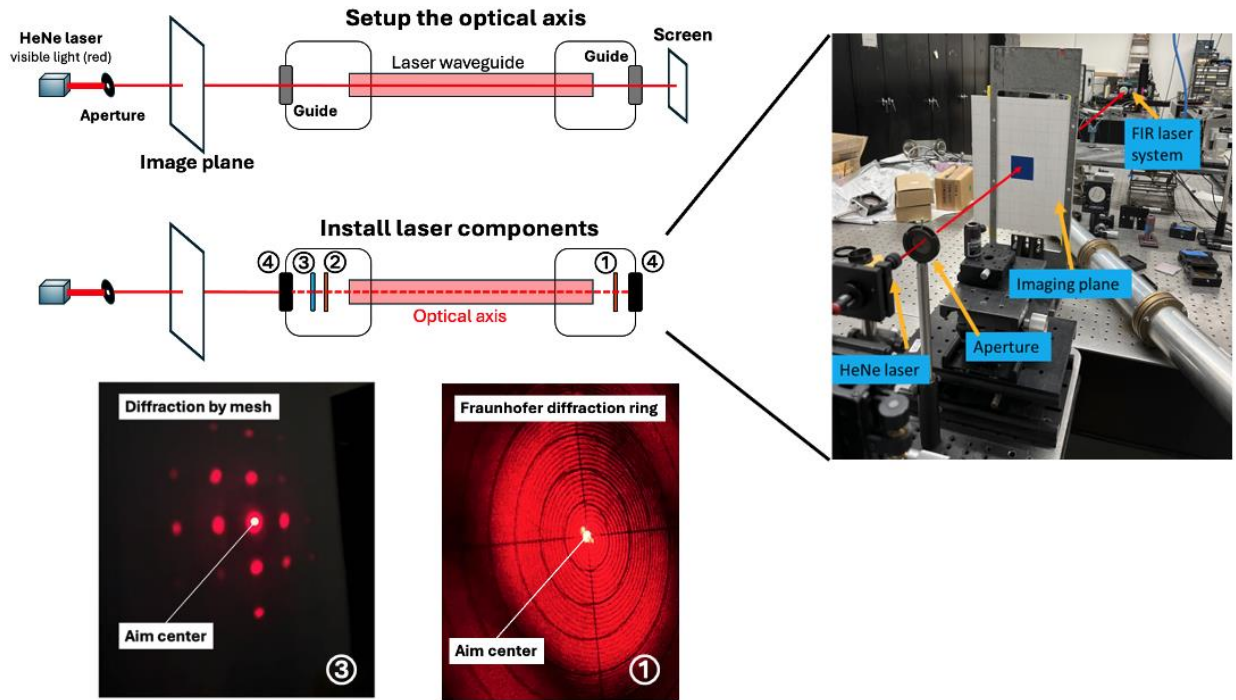

Figure 7. FIR laser alignment procedure showing the optical axis establishment using a HeNe laser through alignment guides, followed by sequential installation: rear mirror (#1, gold-coated copper with CO_2 injection port) aligned via Fraunhofer diffraction pattern centering, front mirror (#2) aligned by reflected spot position, metallic mesh (#3) aligned using zeroth-order diffraction spot, and self-aligning CO_2/FIR windows (#4). Proper alignment verification requires: rear mirror Fraunhofer pattern center and mesh zeroth-order diffraction spot to coincide with the HeNe-established aim center.

The CO_2 laser input and FIR laser output windows (designated # 4 in Fig. 7) are installed as the final components. These windows are automatically aligned through their precise mechanical coupling with the waveguide structure, eliminating the need for active optical alignment. Their fixed mounting position ensures proper orientation while maintaining vacuum integrity and optical transmission properties. With all components now installed, including the rear mirror (#1), front mirror (#2), and metallic mesh (#3) previously aligned using a HeNe laser, the complete FIR laser system achieves optimal configuration for efficient 432 μm radiation generation.

After proper alignment, the FIR laser output beam profile (measured 300 mm from the output window) shows significant improvement compared to the unaligned case, as illustrated in Fig. 8. Without alignment,

the output beam exhibits multiple high-order cavity modes, resulting in a dual-peak intensity distribution with a hollow core along the optical axis. This modal structure degrades coupling efficiency into the transmission line, increasing power insertion losses and causing non-localized scattering in the plasma. Following the alignment procedure described earlier, the beam profile becomes dominated by the fundamental HE_{11} mode, closely approximating a Gaussian distribution. Power measurements using a Scientech Astral AI310 Power Monitor confirmed an output of ~30 mW. At 300 mm from the output window, the fitted Gaussian beam radii were 12.0 mm in both horizontal and vertical directions.

Formic Acid FIR laser beam profiles ($\lambda = 432 \ \mu m, 30 \ mW$)
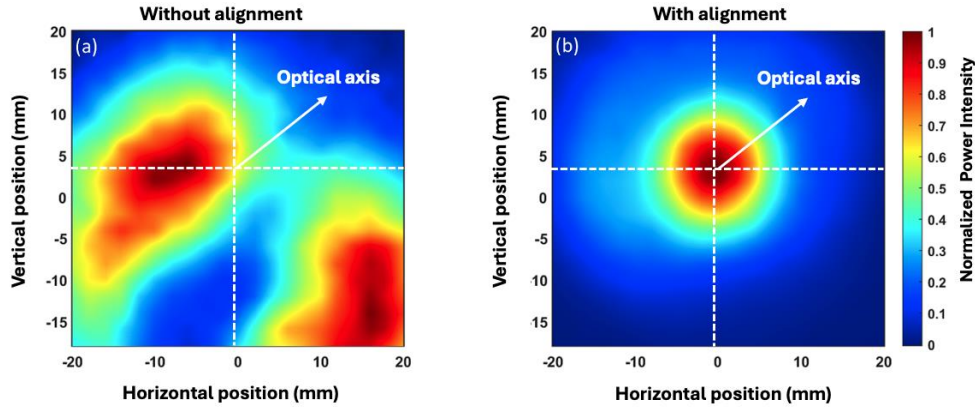**Beam propagation distance = 300 mm**

Figure 8. FIR laser beam profiles at 300 mm from laser output window (a) without alignment; (b) with alignment.

To further characterize the beam, we performed Gaussian fits at multiple propagation distances (940 mm, 1274 mm, 1947 mm, and 2447 mm). As shown in Fig. 9, the aligned beam maintains excellent Gaussian agreement at all positions. Figures 9a and 9b present the horizontal and vertical intensity profiles, respectively, while Figs. 9c and 9d display the corresponding Gaussian radius fits. These curves consistently yield a beam waist size of 10.8 mm, located 0.3 mm behind the output window.

The FIR laser optical alignment typically remains stable for three months or longer under controlled conditions. However, due to the challenging tokamak diagnostics environment, including mechanical vibrations, thermal fluctuations, and potential human interference, a more frequent maintenance schedule is recommended. To ensure optimal performance, the beam profile should be checked every two weeks using Gaussian fitting analysis to verify mode quality. If deviations are observed (e.g., degraded beam symmetry, higher-order mode content, or reduced coupling efficiency), a full realignment should be performed. This proactive approach mitigates diagnostics performance degradation and maintains diagnostics reliability during plasma operations.
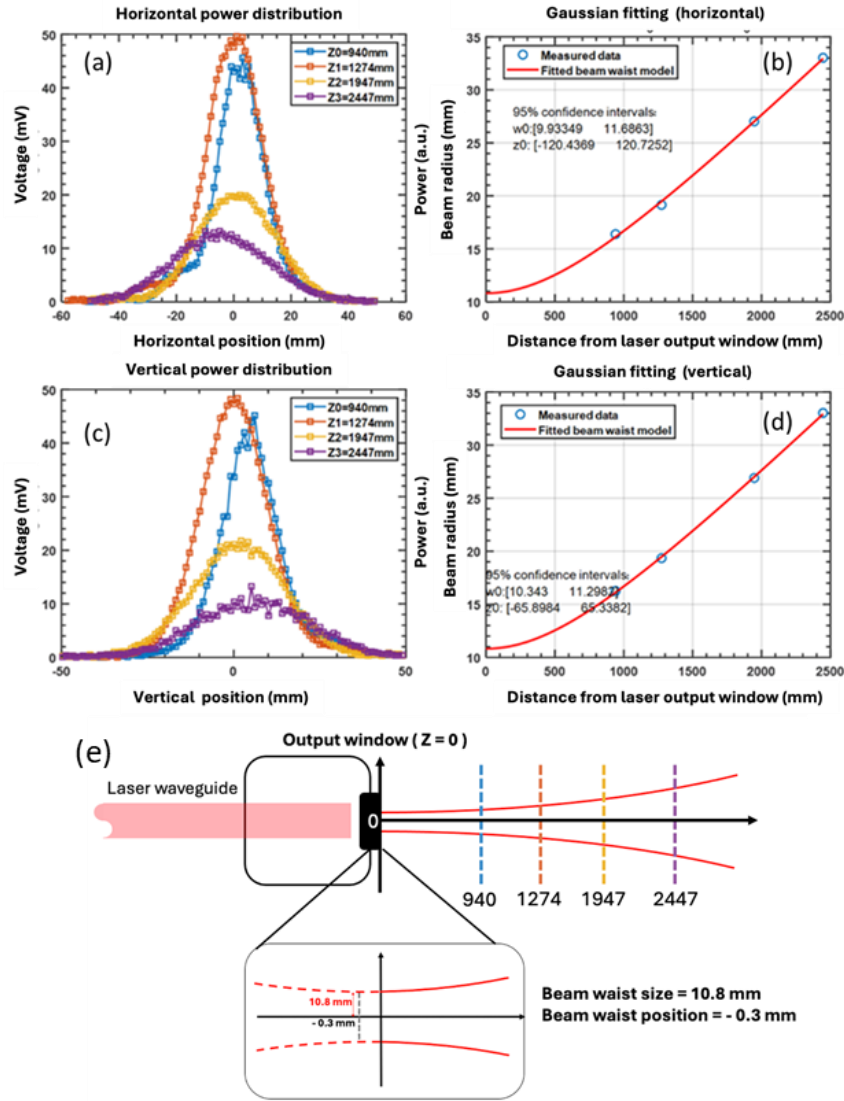
Figure 9. FIR laser output beam characterization. (a) Horizontal beam power distribution profile. (b) Gaussian fit to horizontal profile. (c) Vertical beam power distribution profile. (d) Gaussian fit to vertical profile . (e) Beam waist measurement showing 10.8 mm radius located 0.3 mm behind the output window, as determined by Gaussian fitting analysis.

IV. FIR LASER OUTPUT BEAM POWER OPTIMIZATION

The NSTX-U high-k scattering diagnostic employs a CO_2-pumped formic acid (HCOOH) FIR laser system, which is chosen for its superior spectral purity[31]. This two-stage system produces 432 μm radiation through optical pumping, where the final FIR output power depends critically on both the CO_2 laser pump power and the efficiency of the feed-in coupling system.

To maximize coupling efficiency, we implemented a precision alignment protocol using a visible HeNe laser as a reference beam, accurate enabling of the optical axis establishment for both the infrared CO_2 (9.6 μm) and FIR (432 μm) systems despite their non-visible wavelengths. The alignment procedure

follows the methodology detailed in Sec. III, ensuring optimal overlap between the CO_2 pump beam and the formic acid laser mode. Additionally, the feed-in system incorporates an anti-reflection coated focusing lens (focal length = 1 m at wavelength = 9.6 μm) to increase the CO_2 power density at the FIR laser input, further enhancing the conversion efficiency.

While maximizing power output is important, maintaining stable power output is even more important because it directly impacts the signal level and signal-to-noise ratio of the NSTX-U high-k scattering diagnostics. Ideally, laser output power should remain constant. However, FIR laser power fluctuates due to variations in formic acid gas pressure and thermal expansion-induced cavity length changes. Generally, higher gas pressure reduces peak power but improves robustness against cavity length variations. Through laboratory testing, we identified an optimal operating regime that delivers sufficient output power (>10 mW) while incorporating a cavity length feedback system, significantly improving FIR laser output power stability.

The FIR laser delivers maximum output power when the cavity length satisfies the resonant condition. However, in practice, we observe a gradual decrease in FIR output power over time, as shown in Fig. 10. This monotonic decrease stems from the deterioration of the resonant condition, primarily caused by thermal expansion of the laser cavity, where rising temperatures elongate the cavity length. Consequently, diminishes as operation time increases. As demonstrated in Fig. 9, the FIR laser power drops to half of its initial value within the first 135 seconds of operation. Thus, active feedback control of the cavity length is essential to stabilize power output. To optimize this feedback system, a thorough understanding of the relationship between output power and cavity length adjustment is the beginning.
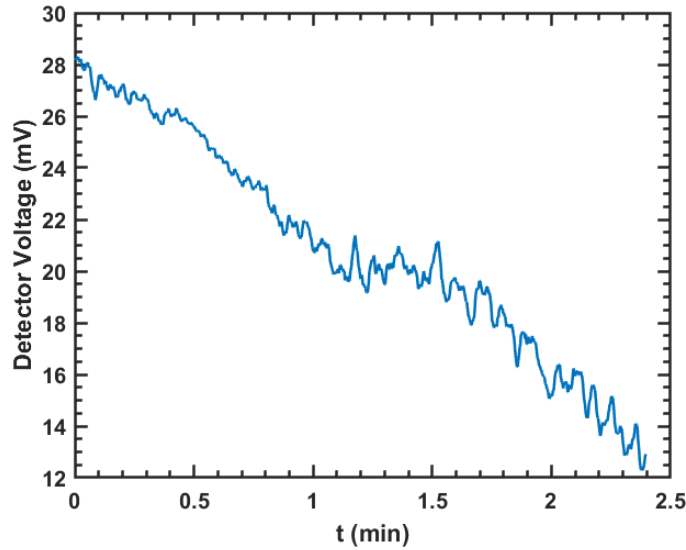

Figure 10. The FIR laser output power's natural temporal decay during operation. This power decrease occurs because thermal expansion gradually alters the cavity length, taking it out of the optimal resonant condition.

As shown in Fig. 11, a computer-controlled stepper motor stage actively adjusts the cavity length. By simultaneously monitoring the FIR laser output power, we establish the precise relationship between cavity length adjustment and power output. Through rapid scanning (under 20 seconds) across 1000

discrete positions within a 2 mm length adjustment range, we obtain the characteristic curve presented in Fig. 12. It shows the variation of FIR laser intensity with controlled cavity length adjustments, defined as cavity shift. The peak-to-peak distance is approximately 216 μm, which is about half of the wavelength ($\lambda_1 = 432.6$ μm). Furthermore, when zooming in on a single peak structure, small fluctuations are observed with a periodicity close to a quarter of the CO_2 laser wavelength ($\lambda_2 = 9.27$ μm). The difference between the FIR and CO_2 laser resonance structures derive from their cavity lengths. For the FIR laser, the resonant space is defined between the metallic mesh and the rear mirror, both of which can be approximated as perfect electric conductors. This results in the boundary condition $k_1 d_1 = n\pi$, leading to a resonance spacing of $\Delta d_1 = \frac{\pi}{k} = \frac{\lambda_1}{2}$, where k_1 is the wavenumber of the FIR laser, n is an integer number, λ_1 represents the FIR wavelength, and d_1 is the FIR laser cavity length. In contrast, for the CO_2 laser, the resonant space is between the front and rear mirrors, with the front mirror being a dielectric wafer. This modifies the resonance condition to $2k_2 d_2 + \phi = n\pi$, where d_2 is the resonant cavity length, k_2 is the wavenumber of the CO_2 laser, and ϕ accounts for the phase shift upon reflection from the front mirror surface. Consequently, the resonance spacing is given by $\Delta d_2 = \frac{\lambda_2}{4}$, where λ_2 represents the CO_2 laser wavelength, which agrees well with the experimental results.
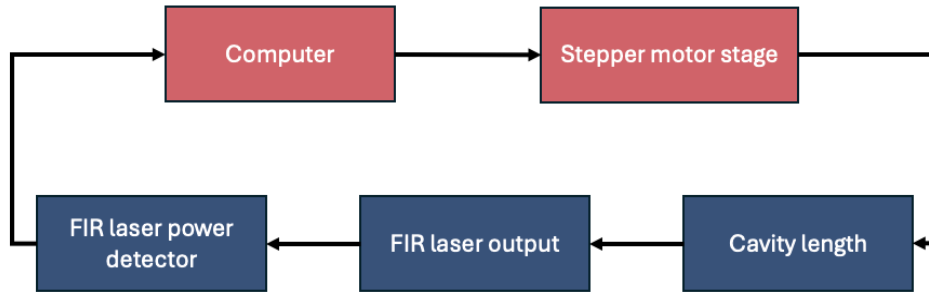

Figure 11. FIR laser cavity alignment setup. The detected FIR laser power is transmitted to a computer, which controls a stepper motor to fine-tune the cavity length and optimize the FIR laser output power.

Based on the established relationship between FIR laser power and cavity length (Fig. 12), we can now implement real-time feedback control. By continuously monitoring output power variations, the system detects cavity length changes induced by thermal expansion and automatically adjusts the position via the stepper motor stage. This active compensation mechanism effectively maintains optimal cavity length and will improve FIR laser power stability during operation.
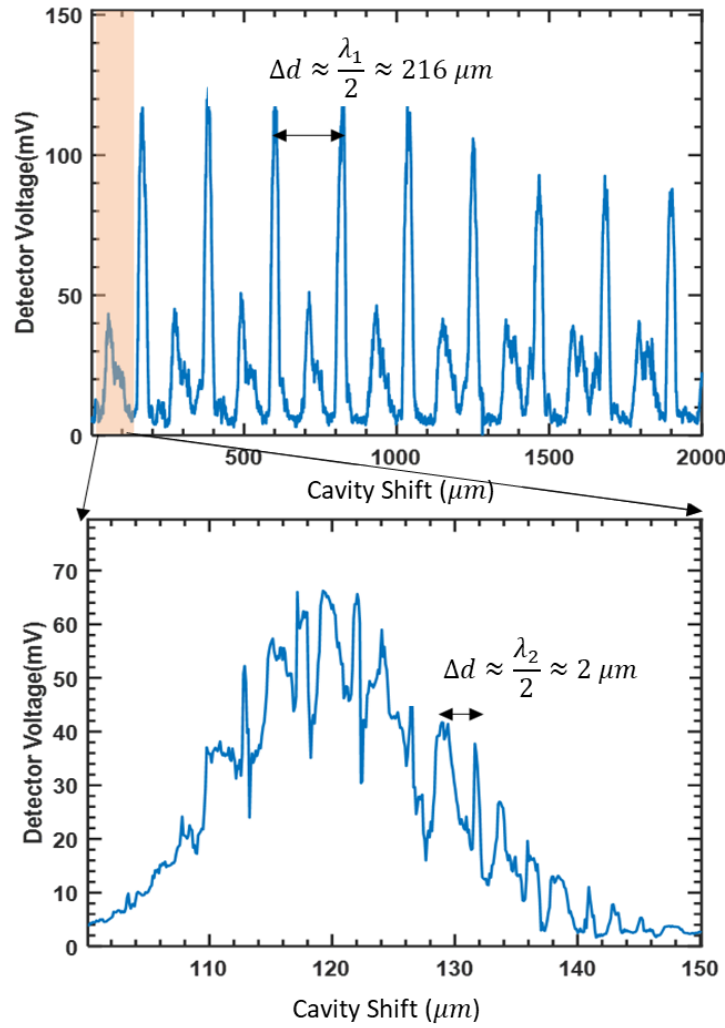
Figure 12. FIR output intensity with cavity shift measured under Formic acid gas pressure around 150 mTorr

Figure 12 reveals that cavity shift-induced FIR output power fluctuations are fundamentally linked to CO_2 laser resonance conditions, creating demanding requirements for the feedback system through both increased adjustment precision and correction frequency. To address these challenges while maintaining output stability, we developed a strategy to smooth the characteristic curve by modifying the CO_2 laser absorption efficiency. Experimental verification, as shown in Fig. 13, demonstrates that increasing formic acid gas pressure from 120-178 mTorr to 190-221 mTorr significantly reduces fluctuation amplitudes in the resonance characteristics. This pressure-dependent behavior confirms that operating at elevated pressures (190-221 mTorr range) provides three key advantages: (1) smoothed power-length dependence that relaxes feedback control requirements, (2) enhanced FIR output stability, and (3) improved system robustness for practical implementation. The results establish gas pressure optimization as an effective approach to mitigate resonance-related fluctuations without compromising system performance. While our experiments demonstrate that higher formic acid gas pressure (190–221 mTorr) effectively smooths cavity-shift-induced power fluctuations (Fig. 13), this improvement comes at the cost of reduced maximum FIR output power. Through systematic testing, we identified 190 mTorr as the optimal operating pressure that achieves the critical balance between stability and performance.
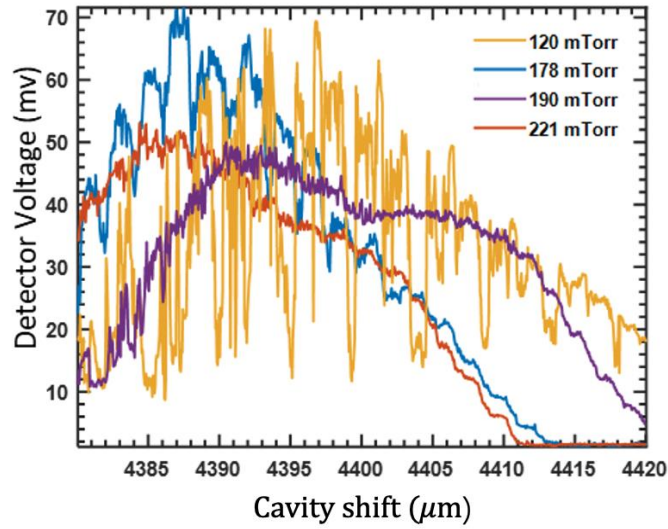
Figure 13. Scanning Cavity under different gas pressures

Since the main resonance structure of the FIR laser will shift to the right due to thermal expansion, this leads to an intensity drop if the cavity remains stationary. To address this, a feedback control system is implemented for automatic cavity optimization. The system continuously monitors the FIR power, and once the intensity drops to 80 % of its original value, it drives the stepper motor to adjust the position of the mesh and front mirror, shifting the cavity to the right to find the optimal position. It operates automatically to maintain the cavity at its optimal position, with each adjustment process taking approximately 10 seconds. With the feedback control system, the output power can be maintained over a long time period, as shown in Fig. 14, where the downward peaks correspond to the auto-adjustment process. The regular adjustment initially occurs approximately every 2 minutes. After about 1 hour, the system reaches thermal stability, and the adjustment interval increases to around 20 minutes.
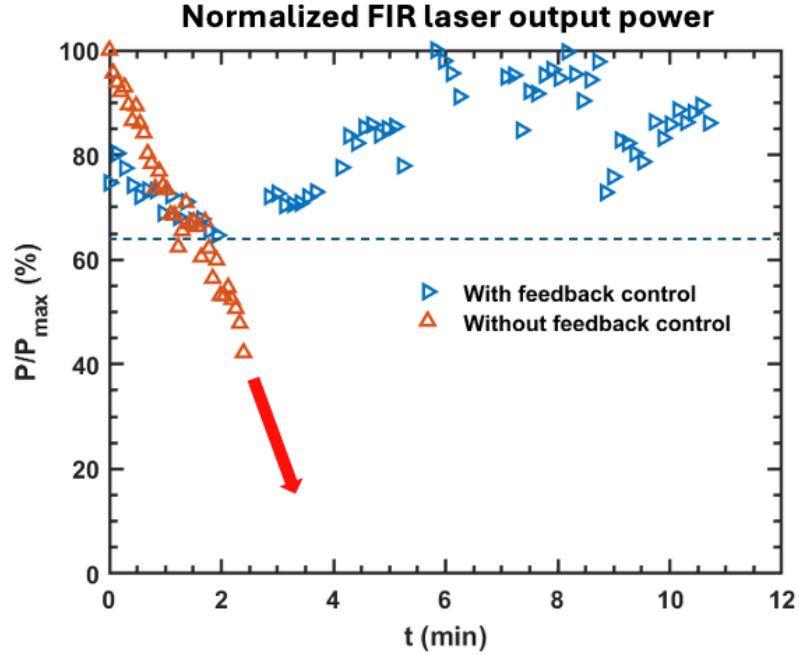
Figure 14. FIR laser intensity evolution with feedback control, where P/P_{max} and P_{max} refers to the maximum power intensity.

V: CONCLUSION

The NSTX-U high-k scattering diagnostic requires a stable 693 GHz FIR laser source delivering ~ 30 mW output with quasi-Gaussian beam profile (10.8 mm waist) and < 20 % power drop during plasma measurements. This work demonstrates a complete optimization solution through: (1) precision optical alignment achieving the Gaussian beam profile, (2) CO_2 pump laser and feed-in system configuration maximizing power output, and (3) an operational balance of 190 mTorr gas pressure with active cavity length feedback control ensuring power stability. The developed techniques, including detailed alignment procedures and stability enhancement methods, provide a replicable framework for other laser-aided diagnostics, offering improved beam quality, higher output power, enhanced output power stability, reduced maintenance requirements, and extended laser system lifetime while lowering operational complexity.

ACKNOWLEDGMENTS

AUTHOR DECLARATIONS

Conflict of Interest

The authors have no conflicts to disclose.

Author Contributions

Xinhang Xu: Conceptualization(equal); Data curation(lead); Formal analysis(lead); Mythology (equal); Validation (lead); Investigation (equal); Writing – original draft (lead). **Jon Dannenberg:** Conceptualization(equal); Mythology (equal); Investigation (equal); Writing – review & editing (equal). **Calvin Domier:** Conceptualization(equal); Mythology (equal); **Yilun Zhu**: Writing – review & editing (equal); Visualization (lead); Funding acquisition(equal). **Xiaoliang Li**: Writing – review & editing (equal). **Neville Luhmann, Jr.**: Writing – review & editing (equal); Supervision (equal); Funding acquisition (equal). **Yang Ren:** Writing – review & editing (equal).

DATA AVAILABILITY

The data that support the findings of this study are available from the corresponding author upon reasonable request.

REFERENCES

1. P. Sun, Y. Ren, W. Wang, X. Han, H. Liu, Y. Li, G. Li, Y. Wang, B. Hao and Y. Zhu, "*On the Role of Ion Temperature Gradient Turbulence in Driving Ion Thermal Transport in Neutral Beam Injection-Heated L-mode Plasmas in a Superconducting Tokamak*", Nuclear Fusion 65, 086014 (2025).

2. Y. Chen, P.-J. Chen, R. Hu, Y. Zhu, J.-H. Yu, A.-V. Pham, O. Momeni, C. Domier, J. Dannenberg and X. Li, "*Frontier system-on-chip (SoC) technology for microwave diagnostics*", Review of Scientific Instruments 95 (9), (2024).

3. M. Ono, S. Kaye, Y.-K. Peng, G. Barnes, W. Blanchard, M. Carter, J. Chrzanowski, L. Dudek, R. Ewig and D. Gates, "*Exploration of spherical torus physics in the NSTX device*", Nuclear Fusion 40 (3Y), 557 (2000).

4. S. Kaye, F. Levinton, D. Stutman, K. Tritz, H. Yuh, M. Bell, R. Bell, C. Domier, D. Gates and W. Horton, "*Confinement and local transport in the National Spherical Torus Experiment (NSTX)*", Nuclear Fusion 47 (7), 499 (2007).

5. Y. Ren, E. Belova, N. Gorelenkov, W. Guttenfelder, S. Kaye, E. Mazzucato, J. Peterson, D. Smith, D. Stutman and K. Tritz, "*Recent progress in understanding electron thermal transport in NSTX*", Nuclear Fusion 57 (7), 072002 (2017).

6. G. Yu, G. Kramer, Y. Zhu, X. Li, Y. Wang, A. Diallo, Y. Ren, J. Yu, Y. Chen and X. Liu, "*Noise suppression for MHD characterization with electron cyclotron emission imaging 1D technique*", Plasma Physics and Controlled Fusion 63 (5), 055001 (2021).

7. G. Yu, G. Kramer, Y. Zhu, M. Austin, S. Denk, M.-G. Yoo, X. Li, B. Zhao, R. Xie and Z. Li, "*Modelling of the electron cyclotron emission burst from a laboratory tokamak plasma with loss-cone maser instability*", Journal of Plasma Physics 90 (6), 985900601 (2024).

8. F. Jenko, W. Dorland, M. Kotschenreuther and B. Rogers, "*Electron temperature gradient driven turbulence*", Physics of plasmas 7 (5), 1904-1910 (2000).

9.   W. Dorland, F. Jenko, M. Kotschenreuther and B. Rogers, "*Electron temperature gradient turbulence*", Physical review letters 85 (26), 5579 (2000).

10.   J. Menard, L. Bromberg, T. Brown, T. Burgess, D. Dix, L. El-Guebaly, T. Gerrity, R. J. Goldston, R. Hawryluk and R. Kastner, "*Prospects for pilot plants based on the tokamak, spherical tokamak and stellarator*", Nuclear Fusion 51 (10), 103014 (2011).

11.   M. Valovič, R. Akers, M. De Bock, J. McCone, L. Garzotti, C. Michael, G. Naylor, A. Patel, C. Roach and R. Scannell, "*Collisionality and safety factor scalings of H-mode energy transport in the MAST spherical tokamak*", Nuclear Fusion 51 (7), 073045 (2011).

12.   C. W. Domier, J. Dannenberg, Y. Zhu, X. Liu, J. R. Sirigiri, Y. Ren, B. Stratton and N. J. r. Luhmann, "*A poloidal high-scattering system for NSTX-U*", Journal of Instrumentation 17 (1), (2022).

13.   R. Barchfeld, C. Domier, Y. Ren, R. Ellis, P. Riemenschneider, N. Allen, R. Kaita, B. Stratton, J. Dannenberg and Y. Zhu, "*The high-k poloidal scattering system for NSTX-U*", Review of Scientific Instruments 89 (10), (2018).

14.   X. Z. Liu, Y. Ren, Y. L. Zhu and N. J. r. Luhmann, "*Quasi-optical beam tracing module development for millimeter-wave high-wavenumber collective scattering on the NSTX-U and EAST tokamaks*", Fusion Eng Des 212, (2025).

15.   P. J. Sun, X. Z. Liu, Y. Ren, G. S. Xu, R. Chen, J. Qian, X. L. Li, C. Domier, J. Dannenberg, K. Yao, Y. L. Zhu and N. J. r. Luhmann, "*Millimeter-wave high-wavenumber scattering diagnostic developments on EAST and NSTX-U*", Review of Scientific Instruments 95 (8), (2024).

16.   X. L. Li, Y. Liu, G. Xu, T. Zhou and Y. Zhu, "*Design and characterization of a single-channel microwave interferometer for the Helicon Physics Prototype eXperiment*", Fusion Engineering and Design 172, 112914 (2021).

17.   X. L. Li, R. Chen, G. S. Xu, C. Domier, X. Z. Liu, Y. W. Zhang, T. F. Zhou, Y. L. Zhu, G. Y. Yu, S. S. Qiu, H. Yu and N. C. Luhmann, "*Development of ultra-short pulse reflectometry on the Experimental Advanced Superconducting Tokamak (EAST)*", Review of Scientific Instruments 95 (7), (2024).

18.   Y. Zhu, J. H. Yu, G. Yu, Y. Ye, B. Tobias, A. Diallo, G. Kramer, Y. Ren, C. W. Domier, X. Li, C. Luo, M. Chen, Y. Chen and N. C. Luhmann, "*W-band system-on-chip electron cyclotron emission imaging system on DIII-D*", Review of Scientific Instruments 91 (9), (2020).

19.   J. C. Hillesheim, W. A. Peebles, T. L. Rhodes, L. Schmitz, A. E. White and T. A. Carter, "*New plasma measurements with a multichannel millimeter-wave fluctuation diagnostic system in the DIII-D tokamak (invited)*", Review of Scientific Instruments 81 (10), (2010).

20.   G. Y. Yu, R. Nazikian, Y. L. Zhu, Y. Zheng, G. Kramer, A. Diallo, Z. Y. Li, X. Chen, D. Ernst, Y. Zheng, M. Austin and N. C. Luhmann, "*ECEI characterization of pedestal fluctuations in quiescent H-mode plasmas in DIII-D*", Plasma Physics and Controlled Fusion 64 (9), (2022).

21.   X. L. Xie, J. Zhou, Y. Zhu, X. M. Pan, H. Zhou, G. Yu, N. C. Luhmann, G. Zhuang and Z. J. Yang, "*Quasi-optical electron cyclotron emission imaging diagnostic advancements on the J-TEXT tokamak*", Fusion Engineering and Design 155, (2020).

22.   J. H. Yu, Y. T. Chang, K. Y. Lin, C. C. Chang, S. F. Chang, Y. Ye, A. V. Pham, B. J. Tobias, Y. Zhu, C. W. Domier and N. C. Luhmann, "*Millimeter-wave system-on-chip advancement for fusion plasma diagnostics*", Review of Scientific Instruments 89 (10), (2018).

23.   Y. Zhu, Y. Chen, J. H. Yu, C. Domier, G. Yu, X. Liu, G. Kramer, Y. Ren, A. Diallo, N. C. Luhmann and X. Li, "*System-on-chip approach microwave imaging reflectometer on DIII-D tokamak*", Review of Scientific Instruments 93 (11), (2022).

24.   R. A. Barchfeld, *Development of Laser Based Plasma Diagnostics for Fusion Research on NSTX-U.* (2017).

25.   C. Domier, Y. Zhu, R. Pereira, J. Steer-Furderer, X. Li, R. Chen, G. Xu, P. Sun and N. Luhmann, "*Ultrashort Pulse Reflectometry (USPR) diagnostic for EAST*", Journal of Instrumentation 17 (02), C02010 (2022).

26.   X. L. Li, Y. Zhu, G. Yu, J. Cao, G. Xu and N. Luhmann, "*High level of integration of front-end imaging optics system for electron cyclotron emission imaging diagnostics on the DIII-D tokamak*", Fusion Engineering and Design 172, 112915 (2021).

27.   Y. Zhu, Y. Chen, J.-H. Yu, C. Domier, G. Yu, X. Liu, G. Kramer, Y. Ren, A. Diallo and N. Luhmann, "*System-on-chip approach microwave imaging reflectometer on DIII-D tokamak*", Review of Scientific Instruments 93 (11), (2022).

28.   Y. Zhu, J.-H. Yu, G. Yu, Y. Ye, Y. Chen, B. Tobias, A. Diallo, G. Kramer, Y. Ren and W. Tang, "*System-on-chip upgrade of millimeter-wave imaging diagnostics for fusion plasma*", Review of scientific instruments 92 (5), (2021).

29.   C. Y. Xiong, J. Chen, Q. Li, Y. Liu and L. Gao, "*A real-time laser feedback control method for the three-wave laser source used in the polarimeter-interferometer diagnostic on Joint-TEXT tokamak*", Review of Scientific Instruments 85 (12), (2014).

30.   M. Perkins and R. Vernon, presented at the IEEE Antennas and Propagation Society International Symposium. Transmitting Waves of Progress to the Next Millennium. 2000 Digest. Held in conjunction with: USNC/URSI National Radio Science Meeting (C, 2000 (unpublished).

31.   S. Jacobsson, "*Optically pumped far infrared lasers*", Infrared physics 29 (5), 853-874 (1989).